Enhancing Thermophotovoltaic Performance Using Graphene-BN-InSb Near-Field Heterostructures

Rongqian Wang, Jincheng Lu, and Jian-Hua Jiang[*]

School of Physical Science and Technology & Collaborative Innovation Center of Suzhou Nano Science and Technology, Soochow University, Suzhou 215006, China

Graphene–hexagonal-boron-nitride–InSb near-field structures are designed and optimized to enhance the output power and energy efficiency of the thermophotovoltaic systems working in the temperature range of common industrial waste heat, from 400 to 800 K, which is also the working temperature range for conventional thermoelectric devices. We show that the highest output electric power can reach 7.6×10^4 W/m^2 for the system with a graphene–hexagonal-boron-nitride heterostructure as the emitter and a graphene-covered InSb p-n junction as the absorber, while the highest energy efficiency is achieved by the system with the heterostructure as the emitter and an uncovered InSb p-n junction as the absorber (reaching to 34% of the Carnot efficiency). These results show that the performances of near-field thermophotovoltaic systems can be comparable with or even superior to state-of-the-art thermoelectric devices. The underlying physics for the significant enhancement of the thermophotovoltaic performance is understood as due to the resonant coupling between the emitter and the p-n junction, where the surface plasmons in graphene and surface-phonon polaritons in boron nitride play crucial roles. Our study provides a stepping stone toward future high-performance thermophotovoltaic systems.

I. INTRODUCTION

Thermophotovoltaic (TPV) cells, as an emergent breed of clean energy resource, have attracted a wide range of research interest due to their potential high performance [1–14]. A TPV system consists of a thermal emitter and an infrared photovoltaic cell that converts thermal radiation into electric power. The emitter can be heated either by the Sun or by industrial waste heat, giving rise to different applications. Far-field thermal radiation is limited by the Stefan-Boltzmann law, resulting in reduced output power, particularly when the temperature of the emitter is below 1000 K. Most of the existing studies are focused on the regime where the emitter has very high temperature, e.g., $T_{emit} > 1000$ K, which corresponds to solar radiation or heat radiation from a secondary thermal emitter that receives the solar radiation energy.

In this work, we focus on the situations where the temperature of the thermal emitter is in the range of common industrial waste heat, 400 K < T_{emit} < 800 K. At such a temperature range, thermal radiation is strongly limited by the Stefan-Boltzmann law, leading to suppressed output power and energy efficiency for the TPV systems. One can turn to the near-field effect [15–22] to enhance thermal radiation flux, which may enable appealing energy efficiency and output power. However, the near-field effect

becomes ineffective if the tunneling through the vacuum gap is inefficient for photons that carry most of the heat energy, i.e., photons of angular frequencies $\omega \sim k_B T_{emit}/\hbar$. One way to overcome this obstacle is to exploit surface-polariton-enhanced near-field radiation [23–27]. Graphene and hexagonal boron nitride (h-BN) provide surface-plasmon polaritons (SPPs) and surface-phonon polaritons (SPhPs) [28–31] due to strong light-matter interactions [32]. These surface polaritons are right in the mid-infrared frequency range that fits the peak radiation frequency of thermal emitters in the temperature range of 400 K < T_{emit} < 800 K. The narrowband-gap indium antimonide (InSb) p-n junction can be used as an effective TPV cell for the conversion of such mid-infrared thermal radiation into electricity. However, there is still a considerable mismatch between the optical property of InSb and that of graphene or h-BN. Such a mismatch significantly reduces the performance of the near-field TPV systems. It has been shown that a sheet of graphene covered on the InSb p-n junction can considerably improve the coupling between the emitter and the TPV cell and thus enhance the near-field thermal radiation [24]. Here, we propose to use h-BN-graphene heterostructures [33–38] as the emitter and the graphene-covered InSb p-n junction as the TPV cell. We find that such a design leads to significantly improved performance as compared to the existing studies [24,39,40]. The main difference between our near-field TPV (NTPV) systems and that in Ref. [24] is that the thermal emitter in our

---

system is made of *h*-BN-graphene heterostructures, making our NTPV systems more powerful or efficient than the NTPV systems considered in Ref. [24], where the emitter is made of bulk *h*-BN.

In this paper, we examine the performances of four different NTPV configurations: (i) the *h*-BN-InSb device (denoted as *h*-BN-InSb, with the monostructure bulk *h*-BN being the emitter and the uncovered InSb *p*-*n* junction being the cell); (ii) the *h*-BN-graphene-InSb device (denoted as *h*-BN-G-InSb, with the bulk *h*-BN being the emitter and the graphene-covered InSb *p*-*n* junction as the cell); (iii) the *h*-BN-graphene-InSb device (denoted as FBN-G-InSb, with the *h*-BN-graphene heterostructure film being the emitter and the uncovered InSb *p*-*n* junction as the cell); and (iv) the *h*-BN-graphene-graphene-InSb device (denoted as FBN-G-G-InSb, with the *h*-BN-graphene heterostructure film being the emitter and the graphene-covered InSb *p*-*n* junction as the cell). We study and compare their performances for various conditions to optimize the performance of the NTPV system and to reveal the underlying physical mechanisms toward high-performance NTPV systems working at the temperature range of 400 K $<T_{\text{emit}}<$ 800 K. Although it has been shown that a single graphene sheet can act as an excellent thermal emitter [23,41], which gives high power density for the NTPV system, such a structure is technologically challenging and the induced energy efficiency is considerably lower than the NTPV systems considered in this work, despite that the power density is comparable with our NTPV systems.

We remark that our findings are consistent with the study in Ref. [42], where the synergy between near-field thermal radiation and inelastic thermoelectricity [43–47] is shown to have considerably improved performance even in the linear-transport regime. On the other hand, our work is also based on the previous studies where the near-field effects are shown to improve the heat radiation flux by orders of magnitude by using infrared hyperbolic metamaterials [33–38].

This paper is structured as follows. In Sec. II, we describe our near-field TPV system, and we introduce the optical properties of the emitter and the InSb cell. We clarify the radiative heat flux exchanged between the emitter and the cell. We also recall the basic formulations of the photoinduced current, electric power, and energy efficiency of the NTPV cell. In Sec. III, we study the performances of the four different NTPV systems at various conditions to search for high-performance NTPV systems. Finally, we summarize and conclude in Sec. IV.

II. SYSTEM AND MODEL

A. Near-field thermal radiation

The proposed NTPV system is presented in Fig. 1. The emitter is a graphene-covered *h*-BN film of thickness *h*,
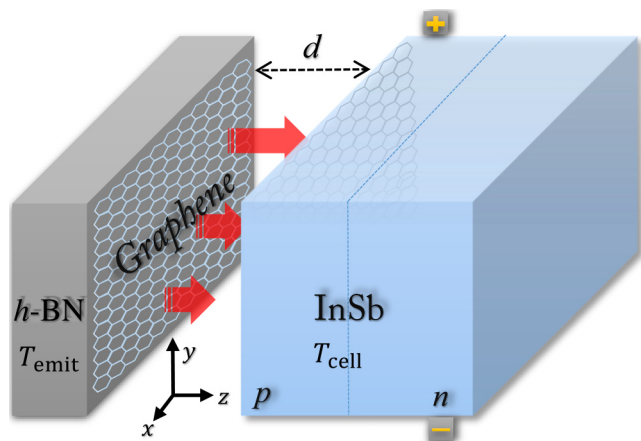

FIG. 1.   Schematic illustration of the NTPV systems. A thermal emitter of temperature T_{emit} made of *h*-BN-graphene heterostructure is placed in the proximity of a thermophotovoltaic cell of temperature T_{cell} made of an InSb *p*-*n* junction. The distance between the emitter and the cell is *d*. The red arrows represent the heat flux radiated from the emitter to the cell. The temperature of the graphene layer attached to the InSb cell (thermal emitter) has the same temperature as the InSb cell (thermal emitter). The coordinate axes on the left side show the in-plane (parallel to the *x*-*y* plane) and out-of-plane (perpendicular to the *x*-*y* plane) directions.

kept at temperature T_{emit}. The TPV cell is made of an InSb *p*-*n* junction, kept at temperature T_{cell}, which is also covered by a layer of graphene. The thermal radiation from the emitter is absorbed by the cell and converted into electricity via infrared photoelectric conversion. In this system, plasmons in graphene can interact strongly with infrared photons and give rise to SPPs. Meanwhile, phonons in *h*-BN can also couple strongly with photons and leads to SPhPs [28,29,31,33–35,48]. These emergent quasiparticles due to strong light-matter interaction can dramatically enhance thermal radiation, particularly via the near-field effect [33–38]. Because of their coincident frequency ranges, the SPPs and SPhPs become hybrid with each other when graphene is placed together with *h*-BN, leading to hybrid polaritons called surface-plasmon-phonon polaritons (SPPPs) [33,34]. SPPPs have been shown to be useful in improving near-field heat transfer between two *h*-BN-graphene heterostructures [36–38]. The radiative heat transfer is optimized when the emitter and absorber are made of the same material, which leads to a resonant energy exchange between the emitter and the absorber [49]. In order to enable such resonant energy exchange in our NTPV cell, we add another layer of graphene onto the InSb cell, as shown in Fig. 1.

The propagation of electromagnetic waves in these materials is described by the Maxwell equations, in which the dielectric functions of these materials are the key factors that determine the propagation of the electromagnetic waves. The dielectric function of *h*-BN is described by a

Drude-Lorentz model, which is given in Ref. [34] as

$$\varepsilon_m = \varepsilon_{\infty,m}\left(1 + \frac{\omega_{\text{LO},m}^2 - \omega_{\text{TO},m}^2}{\omega_{\text{TO},m}^2 - i\gamma_m\omega - \omega^2}\right), \quad (1)$$

where $m = \parallel, \perp$ denotes the out-of-plane and the in-plane directions, respectively. The in-(out-of-)plane direction is determined by whether the electric field is perpendicular (parallel) to the optical axis of the h-BN film (h-BN is a uniaxial crystal, and the optical axis is in the z direction, as defined in Fig. 1). $\varepsilon_{\infty,m}$ is the high-frequency relative permittivity, ω_{TO} and ω_{LO} are the transverse and longitudinal optical phonon frequencies, respectively. γ_m is the damping constant of the optical phonon modes. The values of these parameters are chosen as those determined by experiments [30,50]: $\varepsilon_{\infty,\perp} = 4.87$, $\omega_{\text{TO},\perp} = 1370\,\text{cm}^{-1}$, $\omega_{\text{LO},\perp} = 1610\,\text{cm}^{-1}$, and $\gamma_\perp = 5\,\text{cm}^{-1}$ for in-plane phonon modes and $\varepsilon_{\infty,\parallel} = 2.95$, $\omega_{\text{TO},\parallel} = 780\,\text{cm}^{-1}$, $\omega_{\text{LO},\parallel} = 830\,\text{cm}^{-1}$, and $\gamma_\parallel = 4\,\text{cm}^{-1}$ for out-of-plane phonon modes. There are certain frequency ranges where the in-plane and out-of-plane dielectric functions of h-BN have opposite signs, leading to the hyperbolicity of the isofrequency contour, which makes h-BN a natural hyperbolic metamaterial [34].

The optical property of a graphene sheet is described in this work by a model optical conductivity, σ_g, which consists of both the intraband σ_D and interband σ_I contributions (i.e., $\sigma_g = \sigma_D + \sigma_I$), given respectively in Ref. [51] as

$$\sigma_D = \frac{i}{\omega + i/\tau}\frac{2e^2 k_B T_g}{\pi\hbar^2}\ln\left[2\cosh\left(\frac{\mu_g}{2k_B T_g}\right)\right] \quad (2)$$

and

$$\sigma_I = \frac{e^2}{4\hbar}\left[G\left(\frac{\hbar\omega}{2}\right) + i\frac{4\hbar\omega}{\pi}\int_0^\infty \frac{G(\xi) - G\left(\frac{\hbar\omega}{2}\right)}{(\hbar\omega)^2 - 4\xi^2}d\xi\right], \quad (3)$$

where $G(\xi) = \sinh\left(\xi/k_B T_g\right)/[\cosh\left(\xi/k_B T_g\right) + \cosh(\mu_g/k_B T_g)]$ is a dimensionless function. Here, μ_g is the chemical potential of the graphene sheet, which can be controlled by doping [52,53]. τ is the electron scattering time, which is set as 100 fs in our calculations [35]. T_g is the temperature of the graphene sheet, which is equal to that of the body on which the graphene sheet is attached. e, k_B, and $\hbar$ are the electron charge, Boltzmann constant, and the reduced Planck constant, respectively.

The dielectric function of the InSb cell is given in Ref. [24] as

$$\varepsilon = \left(n + \frac{ic\alpha(\omega)}{2\omega}\right)^2, \quad (4)$$

where $n = 4.12$ is the refractive index and c is the speed of light in vacuum. $\alpha(\omega)$ is a steplike function describing the photonc absorption, which is given by Ref. [24] $\alpha(\omega) = 0$ for $\omega < \omega_{\text{gap}}$ and $\alpha(\omega) = \alpha_0\sqrt{\omega/\omega_{\text{gap}} - 1}$ for $\omega > \omega_{\text{gap}}$ with $\alpha_0 = 0.7\,\mu\text{m}^{-1}$ being the absorption coefficient and

$$\omega_{\text{gap}} = \frac{E_{\text{gap}}}{\hbar} \quad (5)$$

being the angular frequency corresponding to the band gap of InSb. The gap energy E_{gap} of InSb is temperature dependent, and it is given in Ref. [54] as

$$E_{\text{gap}} = 0.24 - 6 \times 10^{-4}\frac{T_{\text{cell}}^2}{T_{\text{cell}} + 500}. \quad (6)$$

In the above equation, the temperature T_{cell} is in unit of kelvins. For instance, for $T_{\text{cell}} = 320$ K, the gap energy $E_{\text{gap}} = 0.17$ eV and the corresponding angular frequency is $\omega_{\text{gap}} = 2.5 \times 10^{14}$ rad/s.

The near-field radiative heat flux exchanged between the emitter and the cell is given in Refs. [55] and [56] as

$$P_{\text{rad}}^{\text{emit}}(\omega) = \frac{\Theta_1\left(T_{\text{emit}}, \omega\right)}{4\pi^2}\sum_j \int kdk\zeta_j\left(\omega, k\right),$$

$$P_{\text{rad}}^{\text{cell}}(\omega) = \frac{\Theta_2\left(T_{\text{cell}}, \omega, \Delta\mu\right)}{4\pi^2}\sum_j \int kdk\zeta_j\left(\omega, k\right),$$

$$P_{\text{rad}}(\omega) = P_{\text{rad}}^{\text{emit}}(\omega) - P_{\text{rad}}^{\text{cell}}(\omega), \quad (7)$$

where $\Theta_1\left(T_{\text{emit}}, \omega\right) \equiv \hbar\omega/[\exp\left(\hbar\omega/k_B T_{\text{emit}}\right) - 1]$ and $\Theta_2\left(T_{\text{cell}}, \omega, \Delta\mu\right) \equiv \hbar\omega/\{\exp\left[(\hbar\omega - \Delta\mu)/k_B T_{\text{cell}}\right] - 1\}$ are the Planck mean oscillator energy of a black body at temperature T_{emit} and T_{cell}, respectively. For $\omega > \omega_{\text{gap}}$, $\Delta\mu$ is the electrochemical potential difference across the p-n junction, which describes the effects of charge injection or depletion on the carrier recombination processes and hence modifies the number of photons through the detailed balance. For $\omega < \omega_{\text{gap}}$, such effects are absent and thus $\Delta\mu$ is set to zero regardless of the actual chemical potential difference. Here, k denotes the magnitude of the in-plane (parallel to the interfaces) wave vector of thermal radiation waves. $\zeta_j(\omega, k)$ is the photon transmission coefficient for the jth polarization ($j = s, p$), which describes the transmittance for a photon with angular frequency ω and wave vector k to traverse the vacuum gap. The transmission coefficient for each polarization consists of the contributions from both the propagating and the

evanescent waves [21],

$$
\zeta_j(\omega, k) = \begin{cases} \dfrac{\left(1 - |r_{\text{emit}}|^2\right)\left(1 - |r_{\text{cell}}|^2\right)}{\left|1 - r_{\text{emit}}^j r_{\text{cell}}^j \exp(2ik_z d)\right|^2}, & k < \dfrac{\omega}{c}, \\[4mm] \dfrac{4\operatorname{Im}\left(r_{\text{emit}}^j\right)\operatorname{Im}\left(r_{\text{cell}}^j\right)\exp(2ik_z d)}{\left|1 - r_{\text{emit}}^j r_{\text{cell}}^j \exp(2ik_z d)\right|^2}, & k > \dfrac{\omega}{c}, \end{cases}
$$

$$(8)$$

where $k_z = \sqrt{\omega^2/c^2 - k^2}$ is the perpendicular-to-plane component of the wave vector in vacuum. r_{emit}^j (r_{cell}^j) with $j = s, p$ is the complex reflection coefficient at the interface between the emitter (cell) and the air. For heterostructure films, such a coefficient is calculated using the scattering matrix approach to take into account the interference effects that play an important role in enhancing the near-field thermal radiation [57],

$$
r_{\text{emit}}^s = \frac{r_{12}^s + \left(1 + r_{12}^s + r_{21}^s\right) r_{23}^s \exp(2ik_{z,2}^s h)}{1 - r_{21}^s r_{23}^s \exp(2ik_{k,2}^s h)}, \quad (9)
$$

$$
r_{\text{cell}}^s = \frac{k_z^s - k_{z,\text{cell}}^s - \mu_0 \sigma_g \omega}{k_z^s + k_{z,\text{cell}}^s + \mu_0 \sigma_g \omega}, \quad (10)
$$

for s polarization and

$$
r_{\text{emit}}^p = \frac{r_{12}^p + \left(1 - r_{12}^p - r_{21}^p\right) r_{23}^p \exp(2ik_{z,2}^p h)}{1 - r_{21}^p r_{23}^p \exp(2ik_{k,2}^p h)}, \quad (11)
$$

$$
r_{\text{cell}}^p = \frac{\varepsilon_{\text{cell}}^{\perp} k_z^p - k_{z,\text{cell}}^p + \dfrac{\sigma_g k_z^p k_{z,\text{cell}}^p}{\varepsilon_0 \omega}}{\varepsilon_{\text{cell}}^{\perp} k_z^p + k_{z,\text{cell}}^p + \dfrac{\sigma_g k_z^p k_{z,\text{cell}}^p}{\varepsilon_0 \omega}} \quad (12)
$$

for p polarization. Here, h is the thickness of the h-BN film in the heterostructure. In our calculation, we adopt $h_{\text{film}} = 20$ nm for optimal performance. The configurations with bulk h-BN as the thermal emitter are also calculated using the above equations where we set a single layer of thickness $h_{\text{bulk}} = 10\,000$ nm to model the bulk h-BN thermal radiation. Following Ref. [36], in the above Eqs. (1)–(3) are the indices for the vacuum region above the h-BN film; the h-BN film region; and the vacuum region below the h-BN film (i.e., the vacuum region between the film and the InSb p-n junction), respectively. $r_{ab}^{s,p}$ is the complex reflection coefficient for photons propagating from the medium a to the medium b ($a, b = 1, 2, 3$) with

either s or p polarization, which is given in Ref. [36] as

$$
r_{ab}^s = \frac{k_{z,a}^s - k_{z,b}^s - \sigma_g \omega \mu_0}{k_{z,a}^s + k_{z,b}^s + \sigma_g \omega \mu_0},
$$

$$
r_{ab}^p = \frac{k_{z,a}^p \varepsilon_b^{\perp} - k_{z,b}^p \varepsilon_a^{\perp} + k_{z,a}^p k_{z,b}^p \dfrac{\sigma_g}{\omega \varepsilon_0}}{k_{z,a}^p \varepsilon_b^{\perp} + k_{z,b}^p \varepsilon_a^{\perp} + k_{z,a}^p k_{z,b}^p \dfrac{\sigma_g}{\omega \varepsilon_0}}. \quad (13)
$$

When there is a graphene layer covered on the interface between the media a and b, the above equation is modified to

$$
r_{ab}^s = \frac{k_{z,a}^s - k_{z,b} - \sigma_g \omega \mu_0}{k_{z,a}^s + k_{z,b} + \sigma_g \omega \mu_0},
$$

$$
r_{ab}^p = \frac{k_{z,a}^p \varepsilon_b^{\perp} - k_{z,b} \varepsilon_a^{\perp} + k_{z,a}^p k_{z,b} \dfrac{\sigma_g}{\omega \varepsilon_0}}{k_{z,a}^p \varepsilon_b^{\perp} + k_{z,b} \varepsilon_a^{\perp} + k_{z,a}^p k_{z,b} \dfrac{\sigma_g}{\omega \varepsilon_0}}. \quad (14)
$$

Here, $k_{z,i}^s = \sqrt{\varepsilon_i^{\perp}(\omega^2/c^2) - k^2}$ and $k_{z,i}^p = \sqrt{\varepsilon_i^{\perp}(\omega^2/c^2) - (\varepsilon_i^{\perp}/\varepsilon_i^{\parallel})k^2}$ ($i = a, b, \text{cell}$) are the z-component wave vectors for media $i = a, b, \text{cell}$ for s and p polarization, respectively. $\varepsilon_i^{\perp}$ and $\varepsilon_i^{\parallel}$ ($i = a, b, \text{cell}$) are the in-plane and out-of-plane components of the relative dielectric tensor. For an isotropic medium like vacuum and InSb, $\varepsilon_1^{\perp} = \varepsilon_1^{\parallel} = \varepsilon_3^{\perp} = \varepsilon_3^{\parallel} = 1$ and $\varepsilon_{\text{cell}}^{\perp} = \varepsilon_{\text{cell}}^{\parallel}$, where the dielectric function of the InSb cell is defined before. ε_0 and μ_0 are the permittivity and permeability of the vacuum, respectively. Throughout this manuscript, the temperature of the graphene layer attached to the InSb cell (thermal emitter) has the same temperature as the InSb cell (thermal emitter). The cell is assumed to be semi-infinite (i.e., much thicker than the wavelength of the absorbed photons $\lesssim 7.5\ \mu$m). The dependence of the energy performance on the cell thickness is beyond the scope of this work.

B. Output power and energy efficiency of near-field thermophotovoltaic cells

When the TPV cell is located at a distance d, which is of the order of or smaller than the thermal wavelength $\lambda_{\text{th}} = 2\pi \hbar c / k_B T_{\text{emit}}$ from the emitter, the thermal radiation can be significantly enhanced due to energy transfer via evanescent waves [23]. The enhanced thermal radiation leads to increased photocurrent and output electric power. The thermal-radiation-induced electric current density is written as [1,58]

$$
I_e = I_{\text{ph}} - I_0 [\exp(V/V_{\text{cell}}) - 1], \quad (15)
$$

where $V = \Delta\mu/e$ is the voltage bias across the TPV cell and $V_{\text{cell}} = k_B T_{\text{cell}}/e$ is the voltage that measures the temperature of the cell [1]. I_{ph} and I_0 are called the photoinduced current density and reverse saturation current

density, respectively. Here, for the sake of simplicity, we consider only the radiative recombination and ignore the nonradiative recombination. Readers can refer to Ref. [59] for a detailed study on the effect of nonradiative recombination on the performance of NTPV cells. The reverse saturation current density (also termed the dark current density) is determined by the diffusion of minority carriers in the InSb p-n junction, which is given by

$$I_0 = e n_i^2 \left(\frac{1}{N_A} \sqrt{\frac{D_e}{\tau_e}} + \frac{1}{N_D} \sqrt{\frac{D_h}{\tau_h}} \right). \qquad (16)$$

Here, $n_i = \sqrt{N_c N_v} \exp[-(E_{\text{gap}}/2k_B T_{\text{cell}})]$ is the intrinsic carrier concentration, which depends on the temperature of the cell, T_{cell} [54]. N_c and N_v are the temperature-dependent effective densities of carriers in the conduction and valence bands, respectively, given by Ref. [54] $N_c = 8 \times 10^{12} \times T_{\text{cell}}^{3/2}$ (cm^{-3}) and $N_v = 1.4 \times 10^{15} \times T_{\text{cell}}^{3/2}$ (cm^{-3}), where the temperature T_{cell} is in units of kelvins. N_A and N_D are the doping densities in the p and n regions, respectively. We adopt the values $N_A = N_D = 10^{19}$ (cm^{-3}). $D_e = 186$ cm^2/s and $D_h = 5.21$ cm^2/s are the diffusion coefficients of the electrons and holes, respectively [41]. τ_e and τ_h are the electron-hole pair recombination time in the n and p regions, respectively. We choose $\tau_e = \tau_h = 1/(5 \times 10^{-26}$ cm^6 s$^{-1}) n_i^2$, as used in Ref. [54]. A more careful treatment of the carrier recombination time may include the near-field-induced enhancement of radiative carrier recombination since the near-field effect leads to a substantial increase of the local photon density of states, which should be considered in future studies.

Following Refs. [24] and [60], the photoinduced current density is given by

$$I_{\text{ph}} = e \int_{\omega_{\text{gap}}}^{\infty} \frac{P_{\text{rad}}(T_{\text{emit}}, T_{\text{cell}}, \omega, \Delta\mu)}{\hbar\omega} d\omega, \qquad (17)$$

where the radiative heat flux spectrum P_{rad} is defined by Eq. (7) in Sec. II A. Here, we assume that all incident photons are absorbed, and each photon with an energy greater than the band gap creates one electron-hole pair; i.e., we assume 100% quantum efficiency, which is a widely adopted approximation in the literature [24,60]. Better treatment can be adopted in future studies, while we focus on the near-field radiation effects due to h-BN and graphene structures in this work.

The output electric power density P_e is defined as the product of the net electric current density and the voltage bias,

$$P_e = -I_e V, \qquad (18)$$

and the energy efficiency η is given by the ratio between the output electric power density P_e and incident radiative heat flux Q_{inc},

$$\eta = \frac{P_e}{Q_{\text{inc}}}, \qquad (19)$$

where the incident radiative heat flux is given by

$$Q_{\text{inc}} = \int_0^{\infty} \frac{d\omega}{4\pi^2} \Theta_1(T_{\text{emit}}, \omega) \sum_j \int k\,dk\,\zeta_j(\omega, k)$$
$$- \int_{\omega_{\text{gap}}}^{\infty} \frac{d\omega}{4\pi^2} \Theta_2(T_{\text{cell}}, \omega, \Delta\mu) \sum_j \int k\,dk\,\zeta_j(\omega, k)$$
$$- \int_0^{\omega_{\text{gap}}} \frac{d\omega}{4\pi^2} \Theta_1(T_{\text{cell}}, \omega) \sum_j \int k\,dk\,\zeta_j(\omega, k). \qquad (20)$$

III. RESULTS AND DISCUSSIONS

A. Performance of the designed NTPV systems

We first examine the optimal performances of the four types of near-field TPV cells [61]. Figure 2 shows the optimal output power and energy efficiency at various vacuum gaps for the four different setups, respectively denoted as h-BN-InSb (bulk h-BN as the emitter and uncovered InSb cell as the receiver), h-BN-G-InSb (bulk h-BN as the emitter and graphene-covered InSb cell as the receiver), FBN-G-InSb (graphene-h-BN heterostructure film as the emitter and uncovered InSb cell as the receiver), and FBN-G-G-InSb (graphene-h-BN heterostructure film as the emitter and graphene-covered InSb cell as the receiver). Throughout this paper, the energy efficiency is in units of the Carnot efficiency,

$$\eta_C = 1 - \frac{T_{\text{cell}}}{T_{\text{emit}}}. \qquad (21)$$

The output power density and energy efficiency are optimized for various physical parameters, including the temperatures of the cell and/or the emitter, the chemical potential of graphene, and the voltage bias across the InSb p-n junction. The optimization is achieved independently for the four different setups. More details of the optimization can be found in Appendix A. The analysis in Appendix A shows that setting $\mu_g = 1.0$ eV, $h_{\text{film}} = 20$ nm, and $T_{\text{cell}} = 320$ K provides roughly optimal performance, both in terms of power and efficiency, for the NTPV systems considered in this work. Therefore, these parameters are kept as those constants in the main text.

Figures 2(a) and 2(b) give the optimal output power and energy efficiency when the temperatures of the cell and the emitter are set as $T_{\text{emit}} = 450$ K and $T_{\text{cell}} = 320$ K. These figures demonstrate some interesting features. First, the optimal output power varies strongly with the vacuum gap d. As d goes below 1 μm, the output power increases
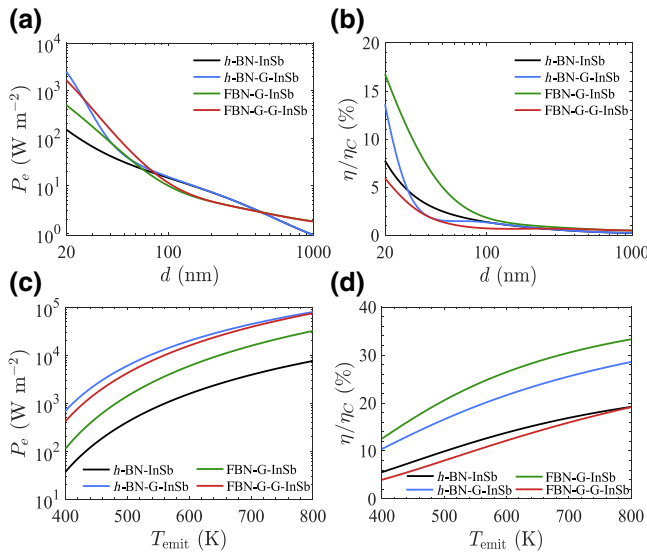
FIG. 2. Optimal performances of the four NTPV devices. (a),(b) Optimal (a) output power density P_e and (b) energy efficiency in units of the Carnot efficiency (η/η_C) as functions of the vacuum gap d. The temperatures of the emitter and the cell are set as $T_{emit} = 450$ K and $T_{cell} = 320$ K, respectively. (c),(d) Optimal (c) output power density P_e and (d) energy efficiency in units of the Carnot efficiency (η/η_C) as functions of the emitter temperature T_{emit} with $d = 20$ nm and $T_{cell} = 320$ K. For all these figures, the chemical potential of graphene is set as $\mu_g = 1.0$ eV. The chemical potential difference across the InSb p-n junction $\Delta\mu$ is optimized independently for each configuration.

dramatically with decreasing d. The best configuration for optimal output power also varies with the vacuum gap d. Close to 1 μm, the configurations with a graphene-h-BN heterostructure as the emitter have the best output power, while for $d < 50$ nm, the output power of the h-BN-G-InSb configuration is also competitive. The energy efficiency also has intriguing features. Most importantly, as shown in Fig. 2(b), the optimal energy efficiency is significantly enhanced for $d < 100$ nm. Dramatically improved energy efficiency at $d = 20$ nm and $\eta = 17\%\eta_C$ for the FBN-G-InSb configuration is much larger than the energy efficiency at $d = 1000$ nm and $\eta \approx 0.5\%\eta_C$. The h-BN-G-InSb configuration also yields appealing energy efficiency. These results demonstrate that graphene, h-BN, and their heterostructure can significantly improve the performance of the TPV cell in the near-field radiation regime.

We study the optimized performance at various temperatures of the thermal emitter T_{emit} in Figs. 2(c) and 2(d). From these figures, we find the following features: the primitive h-BN-InSb setup has poor energy efficiency and output power. With a graphene-covered InSb p-n junction, the h-BN-G-InSb setup has much better energy efficiency and output power. The FBN-G-G-InSb setup achieves the very large output power but with limited energy efficiency, while the FBN-G-InSb setup has the highest energy
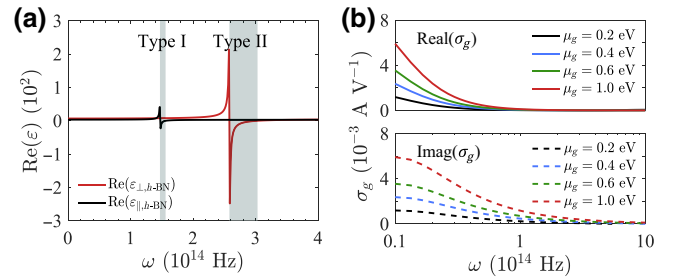

FIG. 3. (a) Real part of the dielectric function ε of h-BN. The two shaded areas represent type I and type II hyperbolic regions of h-BN, respectively. (b) The optical conductivity of graphene σ_g when the temperature of the graphene sheet is set as $T_g = 450$ K.

efficiency and appealing output power. The best output power comes from the h-BN-G-InSb and the FBN-G-G-InSb setups. The overall best performance comes from the h-BN-G-InSb (if high output power is preferred) and the FBN-G-InSb (if high energy efficiency is preferred) setups.

We now elaborate on the microscopic physical mechanisms that give rise to the different characteristics of the four different setups. To achieve such a goal, we first review the optical properties of the bulk h-BN and the graphene. We plot the real part of the relative dielectric functions of the h-BN and the optical conductivity of graphene in Figs. 3(a) and 3(b), respectively. The negativeness of the dielectric functions of the h-BN for the polarizations parallel and perpendicular to the c axis (h-BN is a van der Waals crystal consisting of stacked planar hexagonal boron-nitride sheets along the c axis) defines two frequency regions with strong light-matter interaction. These two regions are termed type I and type II hyperbolic regions, respectively, in the literature [62]. The type I hyperbolic region ranges from 1.5×10^{14} to 1.6×10^{14} rad/s, which is due to the coupling between photons and the optical phonons with displacements along the c axis. The type II hyperbolic region ranges from 2.58×10^{14} to 3.03×10^{14} rad/s due to the strong coupling between the photons and the optical phonons with displacements perpendicular to the c axis. These two hyperbolic regions have different optical properties (e.g., polarization-dependent light propagations) and different isofrequency surfaces [62]. The negativeness of the dielectric function leads to strong reflection and suppressed transmission (often denoted as reststrahlen effects). Such reststrahlen effects are crucial for the enhancement of near-field thermal radiation, because near-field radiation effects are essentially caused by the evanescent propagation of total reflected beams. The reststrahlen effects give rise to frequency ranges with the total reflection for all wave vectors and thus strongly increase the wave-vector space and the number of states with total reflection photons. It has been shown that the reststrahlen effects can

lead to orders-of-magnitude enhancement of the near-field thermal radiation flux [33–38].

Although both reststrahlen bands contribute to the enhancement of near-field radiative energy transfer, it is important to bear in mind that only the higher-frequency reststrahlen band is relevant to energy conversion from thermal radiation to electricity, whereas the lower-frequency reststrahlen band only contributes to wasted (unabsorbed) thermal radiation because the frequency is below the band-gap frequency of the InSb p-n junction, ω_{gap}.

In contrast to the sharp-resonance nature of the optical properties of h-BN, the optical conductivity of the graphene sheet has a broadband feature [63], indicating the broadband dispersion of the graphene plasmons. Figure 3(b) indicates enhanced light-matter interaction with increasing chemical potential. Because of the conical nature of graphene electronic dispersion, the optical properties are identical for positive and negative chemical potentials. In this work, we consider only positive chemical potentials for simplicity.

We now examine the tunnel coupling between the emitter and the absorber by studying the photon transmission coefficient

$$\zeta(\omega, k) \equiv \sum_{j=s,p} \zeta_j(\omega, k) \leq 2 \qquad (22)$$

for the four configurations, using Eq. (8). The photon transmission coefficient as a function of frequency ω and parallel-to-interface wave vector k is shown in Fig. 4 for the four devices at the optimal condition (i.e., with the vacuum gap $d = 20$ nm). The bright regions in these figures represent high photon transmission.

Physically, the high transmission regions correspond to the propagating photonic modes or resonant polaritonic modes due to the evanescently coupled emitter-absorber system. Indeed, as shown in Fig. 4, the high photon transmission regions include the photon propagation region above the light line and the resonance regions below the light line. The former does not include the reststrahlen bands where photon transmission above the light line is suppressed due to the negative dielectric function, which is a common feature for the four devices. The resonance transmission below the light line, which reflects the nature of evanescent coupling between the emitter and absorber, has distinct features for the four devices. The primitive h-BN-InSb device only exhibits enhanced transmission due to the two reststrahlen bands. We find that the type II reststrahlen band has stronger transmission enhancement [see Fig. 4(a)], because this band is above the band-gap frequency of InSb and the evanescent waves in this band can couple resonantly with the electron-hole excitations in the InSb p-n junction.
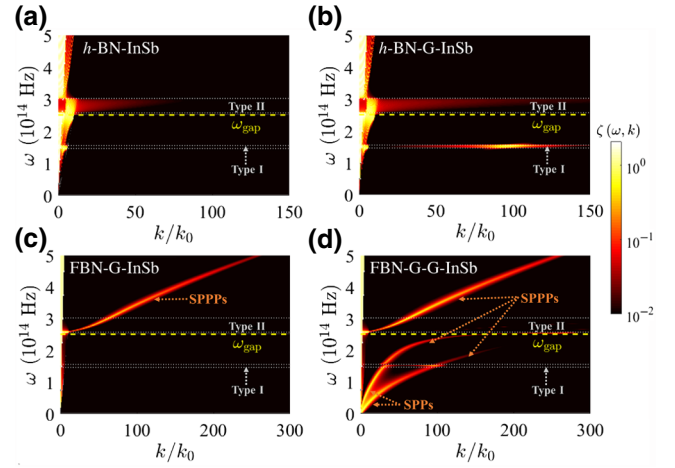

FIG. 4. Photon transmission coefficient $\zeta(\omega, k)$ for (a) h-BN-InSb cell, (b) h-BN-G-InSb cell, (c) FBN-G-InSb cell, and (d) FBN-G-G-InSb cell. The vacuum gap is $d = 20$ nm. The chemical potential of graphene is $\mu_g = 1.0$ eV. Note that the horizontal axis ranges are different for these figures.

When a graphene monolayer is attached to the surface of the InSb junction, the transmission enhancement becomes prominent for larger frequency and wave-vector regions. Because graphene plasmons have a broad frequency band, they can resonantly couple with both the type I and type II reststrahlen bands. These couplings are responsible for the prominent enhancement of the photon transmission in the two reststrahlen bands, as shown in Fig. 4(b). When both the emitter and the absorber are covered by graphene, the evanescent couplings between the emitter and the absorber become more evident. As shown in Fig. 4(d), the high-transmission regions demonstrate the existence of SPPs and SPPPs. The SPPs have two branches, which are due to the evanescent coupling between the two closely spaced graphene layers. Their mutual coupling splits the dispersion of the SPPs. This feature persists to the band-gap frequency of InSb. Above the band gap, the optical properties of the absorber are dominated by the electron-hole excitation in the InSb junction. The high transmission region above the band gap is mainly due to the resonant coupling between the SPPPs and the electron-hole excitation in the InSb junction. The graphene-h-BN heterostructure acts as an efficient near-field thermal emitter due to the SPPPs, which originate from the coupling and hybridization between the SPPs in graphene and the SPhPs in h-BN. Figure 4(c) shows that when the absorber is not covered by graphene, only the SPPP effects above the InSb band gap emerge in the transmission spectrum, because the absorber has no optical absorption below the band gap.

From the above analysis, it becomes clear how the graphene, h-BN, and their heterostructure affect the near-field energy transfer between the emitter and absorber. We now analyze the consequences of the near-field coupling
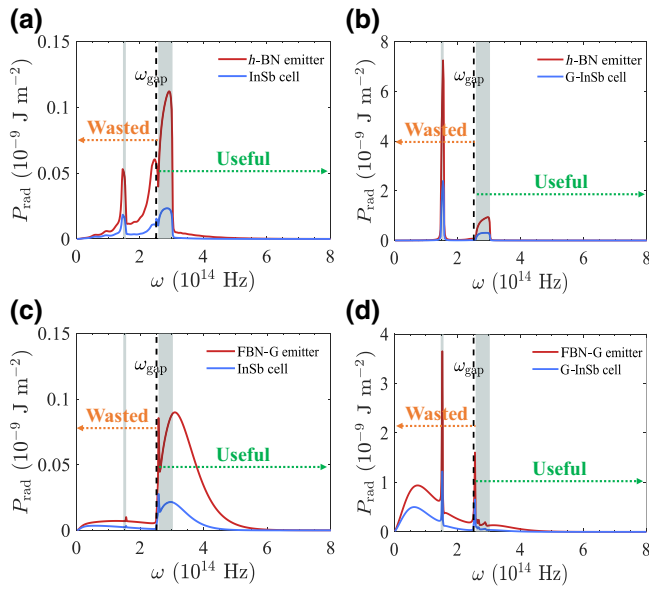
FIG. 5.   Photon emission spectra $P_{rad}(\omega)$ for (a) the h-BN-InSb device, (b) the h-BN-G-InSb device, (c) the FBN-G-InSb device, and (d) the FBN-G-G-InSb device at the maximum output power conditions. The temperatures of the emitter and the cell are kept at $T_{emit} = 450$ K and $T_{cell} = 320$ K, respectively. The vacuum gap is $d = 20$ nm and the chemical potential of graphene is set as $\mu_g = 1.0$ eV. The h-BN film thickness is $h_{film} = 20$ nm for (c) and (d), whereas $h_{film} = 10\,000$ nm for (a) and (b). The chemical potential difference across the InSb p-n junction $\Delta\mu$ is optimized independently for maximum output power for each configuration.

between the emitter and absorber on the performance of the NTPV cells. To achieve this goal, we study the emission spectra $P_{rad}(\omega)$ defined in Eq. (7) for the four devices. In Fig. 5(a), we plot the emission spectra for the emitter and the cell for the h-BN-InSb device. The difference between the two emission spectra gives the net heat exchange flux spectrum. The figure exhibits evidently radiation enhancement at the two reststrahlen bands and the vicinity regions.

Adding graphene to the absorber (i.e., the h-BN-G-InSb device) leads to dramatically enhanced radiative energy transfer both below and above the band gap, as shown in Fig. 5(b) (note that the vertical axes for the four figures have different scales). In contrast, when a graphene-h-BN heterostructure is used as the emitter while a bare InSb junction is used as the absorber (i.e., the FBN-G-InSb device), the enhancement of radiative energy transfer is mainly above the band gap [see Fig. 5(c)]. Such a difference can be understood from the photon transmission spectra in Figs. 4(b) and 4(c). Also, as shown by these figures, the enhancement of photon transmission for the h-BN-G-InSb device is focused on the two reststrahlen bands, while the enhancement of transmission for the FBN-G-G-InSb device has a broadband feature due to the

broadband dispersion of the SPPPs. These characteristics provide a natural explanation of the spectral features in the photon emission in Figs. 5(b) and 5(d). When both the emitter and the absorber are covered with graphene layers, the photon transmissions below and above the band gap are both enhanced. We emphasize that the enhancement of photon emission above the band gap leads to improved output power. In contrast, the enhancement below the band gap leads to reduced energy efficiency, since these photons are useless for energy conversion.

Another feature of the results in Fig. 5 is that the below-band-gap absorption is reduced when compared between Figs. 5(a) and 5(c) [and similarly between Figs. 5(b) and 5(d)]. This feature is due to the fact that thin films of h-BN with 20-nm thickness are used in the setups in Figs. 5(c) and 5(d), whereas much thicker h-BN films with 10 000-nm thickness are used in the setups in Figs. 5(a) and 5(b). The thin h-BN films have much weaker reststrahlen effects compared with the thick h-BN films. Therefore, the near-field thermal radiation in the type I and type II reststrahlen bands are much reduced for the setups in Figs. 5(c) and 5(d). However, since the type II reststrahlen band has stronger coupling with graphene plasmons, the reduction in thermal radiation for the type II reststrahlen band is smaller than that for the type I reststrahlen band. Detailed analysis can be found in Appendix B based on the photon transmission coefficients.

We present the photoinduced current spectra and the incident radiative heat spectra for the four devices in Fig. 6. The narrowband nature of the photoinduced current for the h-BN-G-InSb device and the primitive h-BN-InSb device is clearly shown, while the photoinduced currents for the other two devices exhibit broadband spectra. The incident
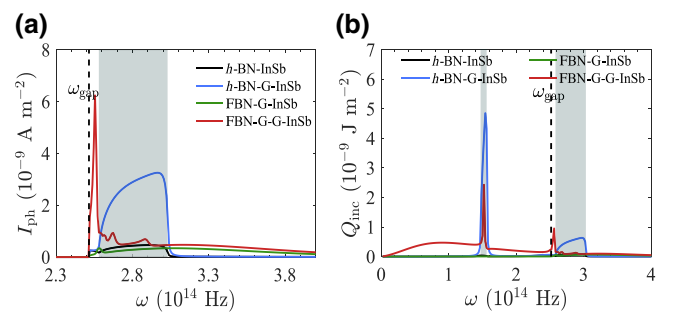

FIG. 6.   (a) Photoinduced current spectra $I_{ph}(\omega)$ and (b) incident radiative heat spectra $Q_{inc}(\omega)$ at the maximum electric power density for the four configurations. The temperatures of the emitter and the cell are kept at $T_{emit} = 450$ K and $T_{cell} = 320$ K, respectively. The vacuum gap is $d = 20$ nm and the chemical potential of graphene is set as $\mu_g = 1.0$ eV. The h-BN film thickness is $h_{film} = 20$ nm for (c) and (d), whereas $h_{film} = 10\,000$ nm for (a) and (b). The chemical potential difference across the InSb p-n junction $\Delta\mu$ is optimized independently for maximum output power for each configuration.

radiative heat spectra illustrate clearly the spectral distributions of the absorbed heat flux for the four devices, which are consistent with the previous analysis.

At this point, it becomes transparent that the FBN-G-InSb and the h-BN-G-InSb devices have better energy efficiency, while the FBN-G-G-InSb and the h-BN-G-InSb devices have better output power. The h-BN-G-InSb benefits from the narrowband nature of photon absorption, which gives rise to improved energy efficiency as compared with broadband photon absorption, as proved in Ref. [42]. In general, those devices are promising for heat-to-electricity energy conversion in the common industry waste-heat regime.

IV. CONCLUSIONS

We investigate the energy efficiency and output power of four different NTPV systems, denoted as the h-BN-InSb device, the h-BN-G-InSb device, the FBN-G-InSb device, and the FBN-G-G-InSb device, where the SPhPs in h-BN and graphene plasmons as well as their couplings play viable roles in improving the energy efficiency and power of those NTPV systems. It is found that the highest output electric power density of 7.6×10^4 W/m^2 is achieved in the FBN-G-G-InSb device, where the graphene-h-BN heterostructure serves as the emitter and the graphene-covered InSb p-n junction serves as the absorber. In contrast, the highest energy efficiency, 34% of the Carnot efficiency, can be realized in the FBN-G-InSb device where the heterostructure serves as the emitter and the bare InSb p-n junction serves as the absorber. Combined with the fact of the experimental availability of the h-BN-graphene heterostructure and the state-of-the-art doping of graphene [52,53], h-BN-graphene–based NTPV systems are appealing for future high-performance heat-to-electricity conversion.

Through those designs, the performance of the NTPV systems can be comparable with the state-of-the-art thermoelectric systems working in the same temperature range. For instance, the state-of-the-art output power density of thermoelectric generators is realized in Ref. [64] with a power factor (PF) PF $= 2.5 \times 10^5$ W/m^2 for a device working between two baths with temperatures $T_h = 873$ K and $T_c = 330$ K. In comparison, the FBN-G-G-InSb device gives PF $= 1.1 \times 10^5$ W/m^2 under the same condition. The state-of-the-art device efficiency of thermoelectric generators is given in Ref. [65], where $\eta = 27\%\eta_C$ for a thermoelectric generator working between two thermal reservoirs with temperatures $T_h = 773$ K and $T_c = 300$ K. The corresponding device figure of merit is $Z_{dev}T = 1.34$. In comparison, the FBN-G-InSb device gives $\eta = 42\%\eta_C$ with a very high device figure of merit of $Z_{dev}T = 3.4$ under the same temperature bias. These comparisons indicate that the NTPV systems studied in this work have competitive performances and thus provide an appealing

pathway toward high-efficiency waste-heat-to-electricity conversion.

APPENDIX A: PERFORMANCES OF THE NTPV SYSTEMS WITH DIFFERENT GRAPHENE CHEMICAL POTENTIALS, CELL TEMPERATURE, AND h-BN FILM THICKNESS

To optimize the performances of the NTPV systems, we tune the chemical potential of the graphene layers, the temperature of the InSb cell, and the thickness of the h-BN films. In this section, we first study the effects of the chemical potential of the graphene layers on the near-field radiation flux, output power, and energy efficiency.

As shown in Fig. 7, the photoinduced current spectrum $I_{ph}(\omega)$ has quite different features for the three NTPV devices with graphene when the chemical potentials of the graphene layers are varied. The chemical potential of graphene can be tuned by doping the graphene
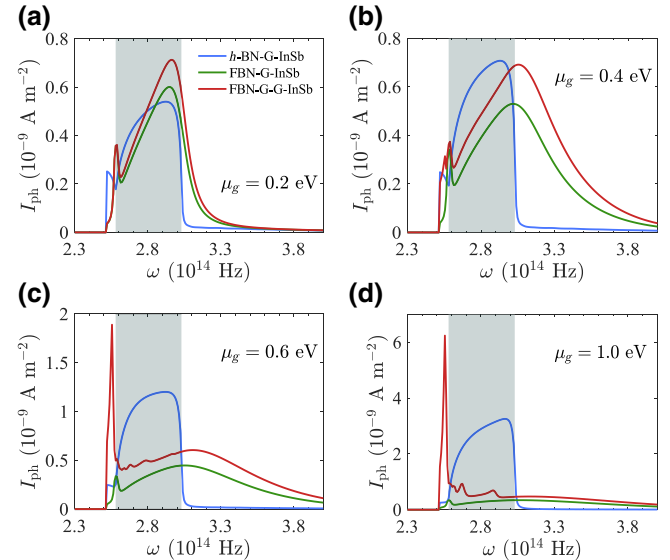

FIG. 7. Effect of the chemical potential of graphene on the photoinduced current spectra for the h-BN-G-InSb cell, FBN-G-InSb cell, and FBN-G-G-InSb cell at (a) $\mu_g = 0.2$ eV, (b) $\mu_g = 0.4$ eV, (c) $\mu_g = 0.6$ eV, and (d) $\mu_g = 1.0$ eV. The temperatures of the emitter and the cell are kept at $T_{emit} = 450$ K and $T_{cell} = 320$ K, respectively. The vacuum gap is $d = 20$ nm. The h-BN film thickness is $h_{film} = 20$ nm for (c) and (d), whereas $h_{film} = 10\,000$ nm for (a) and (b).
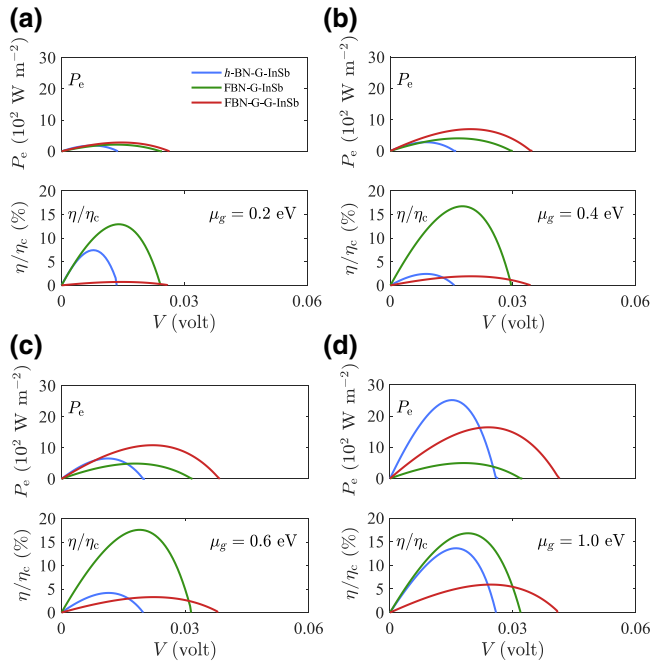
FIG. 8. Effect of the chemical potential of graphene on the performances for the h-BN-G-InSb cell, FBN-G-InSb cell, and FBN-G-G-InSb cell at (a) $\mu_g = 0.2$ eV, (b) $\mu_g = 0.4$ eV, (c) $\mu_g = 0.6$ eV, and (d) $\mu_g = 1.0$ eV. The temperatures of the emitter and the cell are kept at $T_{\text{emit}} = 450$ K and $T_{\text{cell}} = 320$ K, respectively. The vacuum gap is $d = 20$ nm. The h-BN film thickness is $h_{\text{film}} = 20$ nm for (c) and (d), whereas $h_{\text{film}} = 10\,000$ nm for (a) and (b).

FIG. 9. Effect of the h-BN film thickness on the performances for the FBN-G-InSb cell and FBN-G-G-InSb cell at (a) $h_{\text{film}} = 20$ nm, (b) $h_{\text{film}} = 40$ nm, (c) $h_{\text{film}} = 60$ nm, and (d) $h_{\text{film}} = 100$ nm. The temperatures of the emitter and the cell are kept at $T_{\text{emit}} = 450$ K and $T_{\text{cell}} = 320$ K, respectively. The vacuum gap is $d = 20$ nm and the chemical potential of graphene is $\mu_g = 1.0$ eV.

layers [52,53]. As the chemical potential of graphene μ_g increases, the photoinduced current spectrum becomes more and more broadband for the FBN-G-G-InSb and FBN-G-InSb devices. This feature is consistent with the optical properties of graphene (as shown in Fig. 3) and the photon transmission coefficient (as shown in Fig. 4). In contrast, the photoinduced current spectrum $I_{\text{ph}}(\omega)$ of the h-BN-G-InSb device remains to be narrowband, which is focused in the type II reststrahlen band. In this device, the thermal radiation from the h-BN emitter, which is mainly focused in the two reststrahlen bands, is resonantly enhanced by the broadband graphene SPPs in both the type I and type II reststrahlen bands [as shown in Fig. 5(b)]. However, only the type II reststrahlen band contributes to the photoinduced current. Increasing the graphene chemical potential strongly enhances the photoinduced current. The narrowband nature is more preferable for higher energy efficiency, as studied in Ref. [42], making h-BN-G-InSb an attractive device for both energy efficiency and output power. For the FBN-G-G-InSb device (the red curve), the rise of a spike below the type II reststrahlen band with increasing μ_g is due to one branch of the SPPPs that gradually rise to the edge of the type II reststrahlen band, because the group velocities of graphene
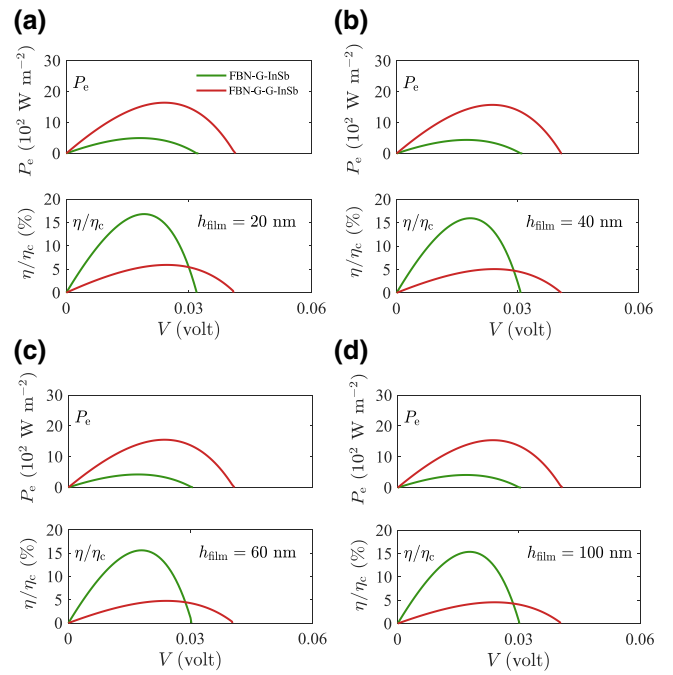
plasmons become larger when the chemical potential increases (see Appendix B for details). Overall, increasing the graphene chemical potential can significantly improve the energy efficiency and output power for the three NTPV devices with graphene, as shown in Fig. 8. We consider $\mu_g = 1.0$ eV in the main text as a large chemical potential that can be obtained in genuine doped graphene [52,53].

The effect of the h-BN film thickness on the performances of the FBN-G-InSb and FBN-G-G-InSb cells are also examined. Figure 9 shows the output power density and energy efficiency of these two NTPV systems for several h-BN film thicknesses. It is found from the figure that the performance of the two NTPV systems is slightly reduced for increasing h-BN film thickness. We thus set the thickness as $h_{\text{film}} = 20$ nm in the main text.

To achieve the optimal performance of the NTPV systems, it is also important to tune the temperature of the InSb cell T_{cell}. The temperature of the InSb cell affects quite a number of physical parameters, including the band gap of the InSb cell, the carrier density, the reverse saturation current (i.e., the dark current), and the open-circuit voltage, to name just a few important quantities. To study the effects of the temperature of the InSb cell, we plot the band-gap frequency of the InSb cell, ω_{gap}; the fraction of useful heat flux (i.e., the exchanged heat flux carried
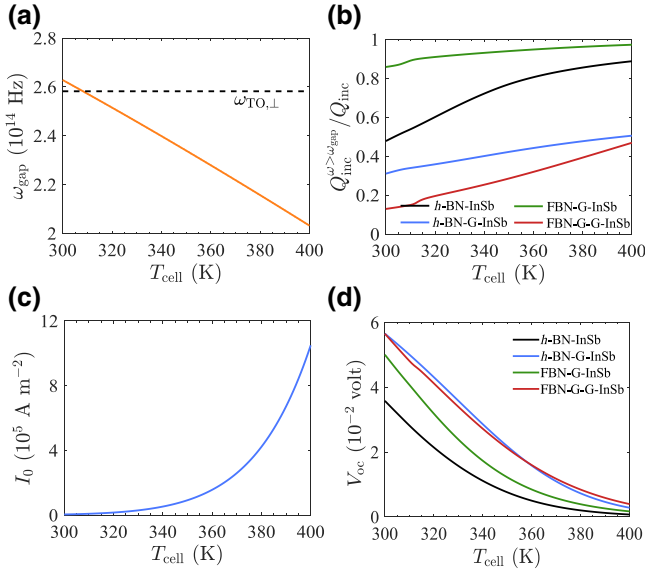
FIG. 10. (a) Band-gap frequency ω_{gap} of the InSb cell, (b) reverse saturation current density I_0, (c) open-circuit voltage V_{oc}, and (d) absorption fractions of incident radiation $P_{\text{inc}}^{\omega>\omega_{\text{gap}}}/P_{\text{inc}}$ at optimal electric power density as functions of the cell temperature T_{cell}. The temperature of the emitter is kept at $T_{\text{emit}} = 450$ K. The vacuum gap is $d = 20$ nm and the chemical potential of graphene is $\mu_g = 1.0$ eV. The h-BN film thickness is $h_{\text{film}} = 20$ nm for (c) and (d), whereas $h_{\text{film}} = 10\,000$ nm for (a) and (b).

by photons with frequency higher than ω_{gap}); the reverse saturation current I_0; and the open-circuit voltage V_{oc} as functions of the temperature of the InSb cell T_{cell} in Fig. 10. From Fig. 10(a), one can see that the band-gap frequency of the InSb cell, ω_{gap}, decreases with increasing temperature T_{cell}. It is important to ensure that the band-gap frequency of the InSb cell is lower than the TO phonon frequency $\omega_{\text{TO},\perp}$ of the h-BN, so that the enhanced near-field thermal radiation in and around the type II reststrahlen band can be fully exploited for the thermophotovoltaic energy conversion. In the main text, we choose T_{cell} to be 320 K to ensure this optimization.

The above consideration is also partly reflected in Fig. 10(b), where the fraction of useful heat flux is plotted as a function of the temperature of the InSb cell. It is seen that this fraction increases with increasing temperature of the InSb cell. Particularly, a visible increase of the fraction of useful heat flux is found around $T_{\text{cell}} = 310$ K, where the band-gap frequency of the InSb cell starts to be smaller than the TO phonon frequency $\omega_{\text{TO},\perp}$ of the h-BN.

On the other hand, the reverse saturation current density I_0 increases strongly with the InSb cell temperature T_{cell}, as shown in Fig. 10(c). This leads to substantially reduced electric current and open-circuit voltage [see Fig. 10(d)] and, hence, reduced output power and energy efficiency. The dramatic increase of the reverse saturation current density is mainly due to the exponential increase of the

carrier density in the p-n junction due to thermal activation across the band gap [see the discussion around Eq. (16)]. Both the increase of the temperature and the reduction of the InSb band gap contribute to the increase of the carrier density. As a consequence, the open-circuit voltages, V_{oc}, decrease with increasing temperature T_{cell}, since $V_{\text{oc}} = V_{\text{cell}} \log\left(I_{\text{ph}}/I_0 + 1\right)$.

To balance these effects, a moderate temperature of the cell has to be adopted. In the main text, we choose the temperature of the InSb cell to be 320 K, which is an optimized value by considering the aforementioned effects. This temperature is also a reasonable value in genuine application scenarios for heat-to-electricity conversion using common industry waste heat.

APPENDIX B: UNDERSTANDING THERMAL RADIATION AROUND THE TYPE-I RESTSTRAHLEN BAND AND THE EFFECTS OF GRAPHENE DOPING ON THE PHOTOCURRENT

In this section, we first use the transmission spectra to understand the thermal radiation around the type I reststrahlen band in Fig. 5. One notable feature in Fig. 5 is that the setups FBN-G-InSb [shown in Fig. 5(c)] and FBN-G-G-InSb [shown in Fig. 5(d)] have much reduced thermal radiation around the type I reststrahlen band, when compared with the setups h-BN-InSb [shown in Fig. 5(a)] and h-BN-G-InSb [shown in Fig. 5(b)]. To understand this feature, we plot in Fig. 11 the transmission spectra around the type I reststrahlen region for the four setups. From the figure, one can see that the transmission around the type I reststrahlen region is much reduced in Figs. 11(c) and
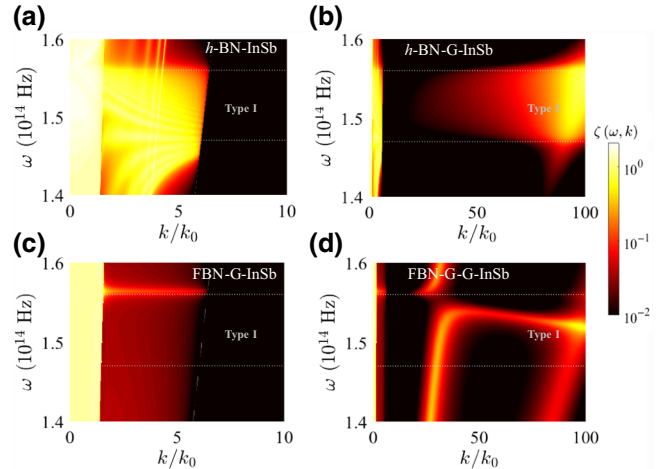

FIG. 11. Transmission spectra around the type I reststrahlen band for (a) the h-BN-InSB setup, (b) h-BN-G-InSb setup, (c) FBN-G-InSb setup, (d) FBN-G-G-InSb setup. The vacuum gap is $d = 20$ nm and the chemical potential of graphene is $\mu_g = 1.0$ eV. The h-BN film thickness is $h_{\text{film}} = 20$ nm for (c) and (d), whereas $h_{\text{film}} = 10\,000$ nm for (a) and (b).
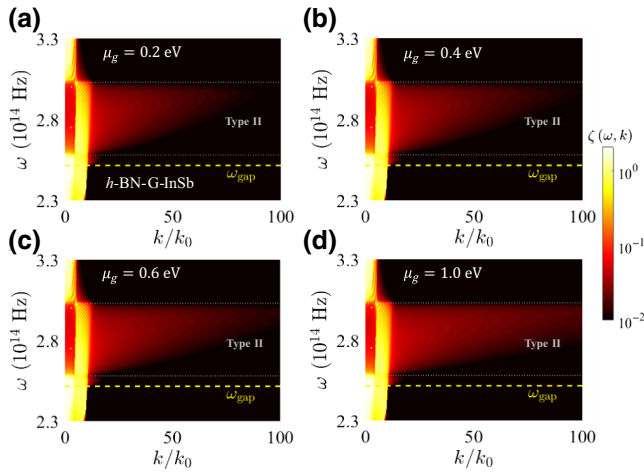
FIG. 12. Transmission spectra around the type II reststrahlen band for (a) h-BN-InSB setup, (b) h-BN-G-InSb setup, (c) FBN-G-InSb setup, (d) FBN-G-G-InSb setup. The vacuum gap is $d = 20$ nm and the chemical potential of graphene is $\mu_g = 1.0$ eV. The h-BN film thickness is $h_{film} = 20$ nm for (c) and (d), whereas $h_{film} = 10\,000$ nm for (a) and (b).

11(d) compared with Figs. 11(a) and 11(b). This property, however, is not due to the attachment of graphene on h-BN (in fact, we find that the attachment of graphene always enhances the thermal radiation, as shown in this work as well as in Ref. [24]), but is due to the fact that h-BN thin films of 20-nm thickness are used in the setups of Figs. 11(c) and 11(d), whereas in the setups of Figs. 11(a) and 11(b), much thicker (10 000-nm) h-BN films are used as thermal emitters. The 20-nm h-BN thin films have much weaker reststrahlen effects and hence

much reduced near-field transmission below the light line. Although adding graphene on top of the thermal emitters can improve the photon transmission, the net effect is still considerably reduced photon transmission around the type I reststrahlen region. This observation explains the reduced thermal radiation around the type I reststrahlen region in Figs. 5(c) and 5(d). In fact, similar features can be observed for the type II reststrahlen region in Figs. 5(c) and 5(d), which, however, is a weaker reduction of thermal radiation compared to that in the type I region. This feature may result from the fact that the type II reststrahlen band has stronger coupling with graphene plasmons, which enhances the near-field thermal radiation and partly compensates the decrease due to the reduced reststrahlen effects.

We now study the photon transmission spectra to understand the photocurrent spectra in Fig. 7 for various graphene doping levels (i.e., electron chemical potential μ_g). The photocurrent increase or decrease is a reflection of the above-band-gap thermal flux increase or decrease. These two quantities are approximately proportional to each other, as indicated by Eq. (17). Therefore, the main features in Fig. 7 reflect that for the h-BN-G-InSb device, the photon transmission is focused in the type II reststrahlen region, while the thermal flux increases with μ_g. For the FBN-G-InSb device, the thermal flux spectrum becomes broader with increase μ_g, while the peak value decreases. Finally, for the FBN-G-G-InSb device, it has similar spectral features as the FBN-G-InSb device for the type II region and above, but with an emerging peak slightly below the type II reststrahlen region. We
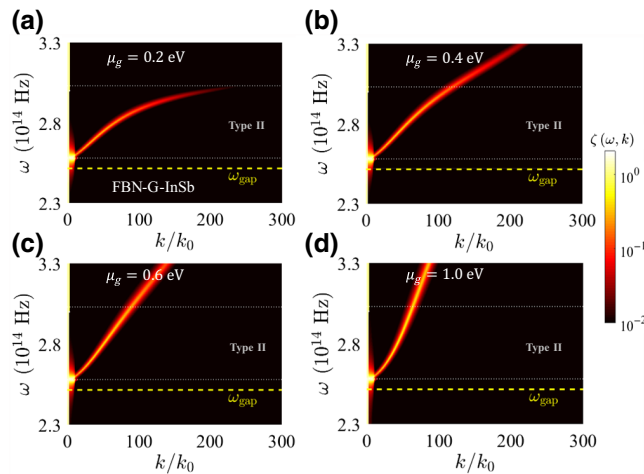

FIG. 13. Transmission spectra around the type II reststrahlen band for (a) h-BN-InSB setup, (b) h-BN-G-InSb setup, (c) FBN-G-InSb setup, (d) FBN-G-G-InSb setup. The vacuum gap is $d = 20$ nm and the chemical potential of graphene is $\mu_g = 1.0$ eV. The h-BN film thickness is $h_{film} = 20$ nm for (c) and (d), whereas $h_{film} = 10\,000$ nm for (a) and (b).

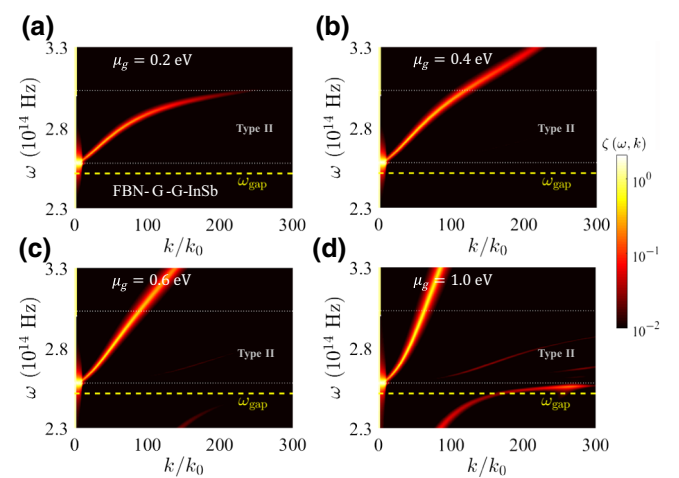FIG. 14. Transmission spectra around the type II reststrahlen band for (a) h-BN-InSB setup, (b) h-BN-G-InSb setup, (c) FBN-G-InSb setup, (d) FBN-G-G-InSb setup. The vacuum gap is $d = 20$ nm and the chemical potential of graphene is $\mu_g = 1.0$ eV. The h-BN film thickness is $h_{film} = 20$ nm for (c) and (d), whereas $h_{film} = 10\,000$ nm for (a) and (b).

now explain these features using the photon transmission spectra in Figs. 12–14.

Figure 12 corresponds to the *h*-BN-G-InSb device. One can see that the enhancement of the photon transmission is always confined to the type II region and nearby. The wave-vector regions with high photon transmission increase substantially with increasing chemical potential μ_g, which, after integration over the wave vector, leads to enhanced thermal radiation flux. Therefore, the feature in Fig. 7 for the *h*-BN-G-InSb device is well understood.

Figure 13 corresponds to the FBN-G-InSb device. The high transmission curve represents the contribution from the SPPPs. The dispersion of the SPPs becomes stronger (i.e., the group velocity becomes larger) when the graphene chemical potential μ_g increases, which is a significant feature of the graphene SPPs [63] (i.e., the group velocity of graphene plasmons becomes larger when the ratio between the energy and the chemical potential μ_g decreases). As a consequence, the frequency region with enhanced thermal radiation becomes broader with increasing μ_g, which leads to broader thermal radiation and absorption spectra. This explains the main feature of the photocurrent spectra for the FBN-G-InSb device.

Figure 14 corresponds to the FBN-G-G-InSb device. The main feature is similar to Fig. 13. However, there is another SPPP branch emerging from the low-frequency region that approaches the the above-band-gap absorption region. This SPPP branch emerges due to the near-field coupling between the SPPs in the two graphene sheets (i.e., the sheet on the emitter and the sheet on the absorber). Such coupling splits the two SPP branches (one from the sheet on the emitter, while the other one from the sheet on the absorber) and leads to a higher-frequency SPP branch and a lower-frequency SPP branch. These SPP branches hybridize with *h*-BN phonons and become SPPPs, which are then limited to the frequency region below the type II reststrahlen region. The higher-frequency SPPP branch approaches the band-gap frequency ω_{gap} at smaller and smaller wave vector as the chemical potential μ_g increases, which is because the group velocity of graphene plasmons becomes larger with increasing μ_g. When such a SPPP branch approaches ω_{gap} at wave vectors smaller than approximately $400k_0$, it will contribute to the near-field radiation. Otherwise, the evanescent-wave decay is too strong, and the photon cannot propagate across the 20-nm vacuum gap. Therefore, the contribution from such a SPPP branch becomes stronger at large chemical potential μ_g, leading to the emergence of a large spike right below the type II reststrahlen region.

---

[1] W. Shockley and H. J. Queisser, Detailed balance limit of efficiency of *p-n* junction solar cells, J. Appl. Phys. **32**, 510 (1961).

[2] R. M. Swanson, Thermophotovoltaic converter and cell for use therein, U.S. Patent 4,234,352 (1980).

[3] L. M. Fraas, J. E. Samaras, P. F. Baldasaro, and E. J. Brown, Spectral control for thermophotovoltaic generators, U.S. Patent 5,403,405 (1995).

[4] S. Wojtczuk, E. Gagnon, L. Geoffroy, and T. Parodos, $In_xGa_{1-x}As$ thermophotovoltaic cell performance vs bandgap, AIP Conf. Proc. **321**, 177 (1995).

[5] R. P. Hamlen, Thermophotovoltaic generator, U.S. Patent 5,560,783 (1996).

[6] T. J. Coutts and M. C. Fitzgerald, Thermophotovoltaics, Sci. Am. **279**, 90 (1998).

[7] D. Martín and C. Algora, Temperature-dependent GaSb material parameters for reliable thermophotovoltaic cell modelling, Semicond. Sci. Tech. **19**, 1040 (2004).

[8] T. Nagashima, K. Okumura, and M. Yamaguchi, A germanium back contact type thermophotovoltaic cell, AIP Conf. Proc. **890**, 174 (2007).

[9] L. M. Fraas and L. G. Ferguson, Three-layer solid infrared emitter with spectral output matched to low bandgap thermophotovoltaic cells, U.S. Patent 6,091,018 (2000).

[10] O. V. Sulima and A. W. Bett, Fabrication and simulation of GaSb thermophotovoltaic cells, Sol. Energy Mater. Sol. Cells **66**, 533 (2001).

[11] C. Wu, B. Neuner III, J. John, A. Milder, B. Zollars, S. Savoy, and G. Shvets, Metamaterial-based integrated plasmonic absorber/emitter for solar thermo-photovoltaic systems, J. Opt. **14**, 024005 (2012).

[12] W. R. Chan, P. Bermel, R. C. N. Pilawa-Podgurski, C. H. Marton, K. F. Jensen, J. J. Senkevich, J. D. Joannopoulos, M. Soljačić, and I. Celanovic, Toward high-energy-density, high-efficiency, and moderate-temperature chip-scale thermophotovoltaics, Proc. Nat. Acad. Sci. **110**, 5309 (2013).

[13] T. Liao, L. Cai, Y. Zhao, and J. Chen, Efficiently exploiting the waste heat in solid oxide fuel cell by means of thermophotovoltaic cell, J. Power Sources **306**, 666 (2016).

[14] E. Tervo, E. Bagherisereshki, and Z. M. Zhang, Near-field radiative thermoelectric energy converters: A review, Front. Energy **12**, 5 (2018).

[15] E. G. Cravalho, C. L. Tien, and R. P. Caren, Effect of small spacings on radiative transfer between two dielectrics, J. Heat Transfer **89**, 351 (1967).

[16] J. B. Xu, K. Lauger, K. Dransfeld, and I. H. Wilson, Thermal sensors for investigation of heat transfer in scanning probe microscopy, Rev. Sci. Instrum. **65**, 2262 (1994).

[17] J. Xu, B. Koslowski, R. Möller, K. Läuger, K. Dransfeld, and I. H. Wilson, Proposal to study the thermopower produced by a vacuum-tunneling junction, J. Vac. Sci. Technol. B **12**, 2156 (1994).

[18] J. B. Xu, K. Läuger, R. Möller, K. Dransfeld, and I. H. Wilson, Energy-exchange processes by tunneling electrons, Appl. Phys. A **59**, 155 (1994).

[19] J. B. Xu, K. Läuger, R. Möller, K. Dransfeld, and I. H. Wilson, Heat transfer between two metallic surfaces at small distances, J. Appl. Phys. **76**, 7209 (1994).

[20] A. I. Volokitin and B. N. J. Persson, Radiative heat transfer between nanostructures, Phys. Rev. B **63**, 205404 (2001).

[21] J. P. Mulet, K. Joulain, R. Carminati, and J. J. Greffet, Enhanced radiative heat transfer at nanometric distances, Microscale Thermophys. Eng. **6**, 209 (2002).

[22] L. Hu, A. Narayanaswamy, X. Chen, and G. Chen, Near-field thermal radiation between two closely spaced glass plates exceeding planck's blackbody radiation law, Appl. Phys. Lett. **92**, 133106 (2008).

[23] O. Ilic, M. Jablan, J. D. Joannopoulos, I. Celanovic, and M. Soljačić, Overcoming the black body limit in plasmonic and graphene near-field thermophotovoltaic systems, Opt. Express **20**, A366 (2012).

[24] R. Messina and P. Ben-Abdallah, Graphene-based photovoltaic cells for near-field thermal energy conversion, Sci. Rep. **3**, 1383 (2013).

[25] B. Wang, X. Zhang, X. Yuan, and J. Teng, Optical coupling of surface plasmons between graphene sheets, Appl. Phys. Lett. **100**, 131111 (2012).

[26] V. B. Svetovoy, P. J. Van Zwol, and J. Chevrier, Plasmon enhanced near-field radiative heat transfer for graphene covered dielectrics, Phys. Rev. B **85**, 155418 (2012).

[27] V. B. Svetovoy and G. Palasantzas, Graphene-on-silicon Near-field Thermophotovoltaic Cell, Phys. Rev. Appl. **2**, 034006 (2014).

[28] S. Dai, Z. Fei, Q. Ma, A. S. Rodin, M. Wagner, A. S. McLeod, M. K. Liu, W. Gannett, W. Regan, K. Watanabe, T. Taniguchi, M. Thiemens, G. Dominguez, A. H. Castro Neto, A. Zettl, F. Keilmann, P. Jarillo-Herrero, M. M. Fogler, and D. N. Basov, Tunable phonon polaritons in atomically thin van der waals crystals of boron nitride, Science **343**, 1125 (2014).

[29] X. G. Xu, B. G. Ghamsari, J.-H. Jiang, L. Gilburd, G. O. Andreev, C. Zhi, Y. Bando, D. Golberg, P. Berini, and G. C. Walker, One-dimensional surface phonon polaritons in boron nitride nanotubes, Nature Commun. **5**, 4782 (2014).

[30] J. D. Caldwell, A. V. Kretinin, Y. Chen, V. Giannini, M. M. Fogler, Y. Francescato, C. T. Ellis, J. G. Tischler, C. R. Woods, A. J. Giles, M. Hong, K. Watanabe, T. Taniguchi, S. A. Maier, and K. S. Novoselov, Sub-diffractional volume-confined polaritons in the natural hyperbolic material hexagonal boron nitride, Nature Commun. **5**, 5221 (2014).

[31] X. G. Xu, J.-H. Jiang, L. Gilburd, R. G. Rensing, K. S. Burch, C. Zhi, Y. Bando, D. Golberg, and G. C. Walker, Mid-infrared polaritonic coupling between boron nitride nanotubes and graphene, Acs Nano **8**, 11305 (2014).

[32] J.-H. Jiang and S. John, Photonic Crystal Architecture for Room-temperature Equilibrium Bose-einstein Condensation of Exciton Polaritons, Phys. Rev. X **4**, 031025 (2014).

[33] V. W. Brar, M. S. Jang, M. Sherrott, S. Kim, J. J. Lopez, L. B. Kim, M. Choi, and H. Atwater, Hybrid surface-phonon-plasmon polariton modes in graphene/monolayer h-bn heterostructures, Nano Lett. **14**, 3876 (2014).

[34] A. Kumar, T. Low, K. H. Fung, P. Avouris, and N. X. Fang, Tunable light-matter interaction and the role of hyperbolicity in graphene-hBN system, Nano Lett. **15**, 3172 (2015).

[35] A. Woessner, M. B. Lundeberg, Y. Gao, A. Principi, P. Alonso-González, M. Carrega, K. Watanabe, T. Taniguchi, G. Vignale, M. Polini, J. Hone, R. Hillenbrand, and F. H. L. Koppens, Highly confined low-loss plasmons in graphene-boron nitride heterostructures, Nat. Mater. **14**, 421 (2015).

[36] B. Zhao and Z. M. Zhang, Enhanced photon tunneling by surface plasmon–phonon polaritons in graphene/hBN heterostructures, J. Heat Transfer **139**, 022701 (2015).

[37] B. Zhao, B. Guizal, Z. M. Zhang, S. Fan, and M. Antezza, Near-field heat transfer between graphene/hBN multilayers, Phys. Rev. B **95**, 245437 (2017).

[38] K. Shi, F. Bao, and S. He, Enhanced near-field thermal radiation based on multilayer graphene-hbn heterostructures, ACS Photonics **4**, 971 (2017).

[39] O. S. Heavens, *Optical Properties of Thin Solid Films* (Courier Corporation, Chicago, 1991).

[40] Z. Knittl, *Optics of Thin Films: An Optical Multilayer Theory* (Wiley London, London, 1976).

[41] M. Lim, S. Jin, S. S. Lee, and B. J. Lee, Graphene-assisted Si—InSb thermophotovoltaic system for low temperature applications, Opt. Express **23**, A240 (2015).

[42] J.-H. Jiang and Yoseph Imry, Near-field three-terminal thermoelectric heat engine, Phys. Rev. B **97**, 125422 (2018).

[43] J.-H. Jiang, O. Entin-Wohlman, and Y. Imry, Thermoelectric three-terminal hopping transport through one-dimensional nanosystems, Phys. Rev. B **85**, 075412 (2012).

[44] J.-H. Jiang, O. Entin-Wohlman, and Y. Imry, Hopping thermoelectric transport in finite systems: Boundary effects, Phys. Rev. B **87**, 205420 (2013).

[45] J.-H. Jiang, Enhancing efficiency and power of quantum-dots resonant tunneling thermoelectrics in three-terminal geometry by cooperative effects, J. Appl. Phys. **116**, 194303 (2014).

[46] J.-H. Jiang, Three-terminal semiconductor junction thermoelectric devices: Improving performance, New J. Phys. **15**, 075021 (2013).

[47] J.-H. Jiang and Y. Imry, Enhancing Thermoelectric Performance Using Nonlinear Transport Effects, Phys. Rev. Appl. **7**, 064001 (2017).

[48] J.-H. Jiang, X. G. Xu, L. Gilburd, and G. C. Walker, Optical hot-spots in boron-nitride nanotubes at mid infrared frequencies: One-dimensional localization due to random-scattering, Opt. Express **25**, 25059 (2017).

[49] K. Joulain, J.-P. Mulet, F. Marquier, R. Carminati, and J.-J. Greffet, Surface electromagnetic waves thermally excited: Radiative heat transfer, coherence properties and casimir forces revisited in the near field, Surf. Sci. Rep. **57**, 59 (2005).

[50] R. Geick, C. H. Perry, and G. Rupprecht, Normal modes in hexagonal boron nitride, Phys. Rev. **146**, 543 (1966).

[51] L. A. Falkovsky, Optical properties of graphene, J. Phys.: Conf. Ser. **129**, 012004 (2008).

[52] G. Lu, T. Wu, P. Yang, Y. Yang, Z. Jin, W. Chen, S. Jia, H. Wang, G. Zhang, J. Sun, Pulickel M. Ajayan, J. Lou, X. Xie, and M. Jiang, Synthesis of high-quality graphene and hexagonal boron nitride monolayer in-plane heterostructure on Cu—Ni alloy, Adv. Sci. **4**, 1700076 (2017).

[53] S. Zhang, J. Li, H. Wu, X. Li, and W. Guo, Direct synthesizing in-plane heterostructures of graphene and hexagonal boron nitride in designed pattern, Adv. Mater. Interfaces **5**, 1800208 (2018).

[54] M. S. Shur, *Handbook Series on Semiconductor Parameters* (World Scientific, Singapore, 1996).

[55] D. V. H. M. Polder and M. Van Hove, Theory of radiative heat transfer between closely spaced bodies, Phys. Rev. B **4**, 3303 (1971).

[56] J. B. Pendry, Radiative exchange of heat between nanostructures, J. Phys.: Condens. Matter **11**, 6621 (1999).

[57] Z. M. Zhang, *Nano/Microscale Heat Transfer* (McGraw-Hill, New York, 2007).

[58] N. W. Ashcroft and N. D. Mermin, *Solid State Physics* (Cengage Learning, Philadelphia, 1976).

[59] B. Zhao, K. Chen, S. Buddhiraju, G. Bhatt, M. Lipson, and S. Fan, High-performance near-field thermophotovoltaics for waste heat recovery, Nano Energy **41**, 344 (2017).

[60] M. Laroche, R. Carminati, and J. J. Greffet, Near-field thermophotovoltaic energy conversion, J. Appl. Phys. **100**, 063704 (2006).

[61] A. Karalis and J. D. Joannopoulos, Transparent and 'opaque'conducting electrodes for ultra-thin highly-efficient near-field thermophotovoltaic cells, Sci. Rep. **7**, 14046 (2017).

[62] Z. Jacob, Nanophotonics: Hyperbolic phonon-polaritons, Nat. Mater. **13**, 1081 (2014).

[63] G. Yin, J. Yang, and Y. Ma, Near-field heat transfer between graphene monolayers: Dispersion relation and parametric analysis, Appl. Phys. Express **9**, 122001 (2016).

[64] R. He, D. Kraemer, J. Mao, Q. Zeng, L. Jie, Y. Lan, C. Li, J. Shuai, H. S. Kim, Y. Liu, D. Broido, C.-W. Chu, G. Chen, and Z. Ren, Achieving high power factor and output power density in p-type half-heuslers $Nb_{1-x}Ti_xFeSb$, Proc. Nat. Acad. Sci. **113**, 13576 (2016).

[65] L.-D. Zhao, G. Tan, S. Hao, J. He, Y. Pei, H. Chi, H. Wang, S. Gong, H. Xu, V. P. Dravid, C. Uher, G. J. Snyder, C. Wolverton, and M. G. Kanatzidis, Ultrahigh power factor and thermoelectric performance in hole-doped single-crystal SnSe, Science **351**, 141 (2016).